Acta Materialia 309 (2026) 122063

Contents lists available at ScienceDirect

Acta Materialia

journal homepage: www.elsevier.com/locate/actamat

Full length article

Corrosion-resistant coatings in molten salts suggested by computational phase-stability diagrams

Seongwon Ham [a,1], Choah Kwon [a,b,1], Minho Kim [a], Han Lim Cha [c], Ho-A Kim [a], Jong-Il Yun [d], Jun Woo Park [d], Jongwoo Lee [a,e], SeungYop Paek [e], Jinsuo Zhang [f], Ju Li [b,g,*], Sangtae Kim [a,h,*]

[a] Department of Nuclear Engineering, Hanyang University, Seoul, 04763, South Korea
[b] Department of Nuclear Science and Engineering, Massachusetts Institute of Technology, Cambridge, MA 02139, USA
[c] Nuclear Chemistry Technology Division, Korea Atomic Energy Research Institute, Daejeon, 34057, South Korea
[d] Department of Nuclear and Quantum Engineering, Korea Advanced Institute of Science and Technology, Daejeon, 34141, South Korea
[e] NewEnergy Division, Hyundai E&C, Seoul, 03058, South Korea
[f] Nuclear Engineering Program, Department of Mechanical Engineering, Virginia Polytechnic Institute and State University, Blacksburg, VA, 24061, USA
[g] Department of Materials Science and Engineering, Massachusetts Institute of Technology, Cambridge, MA, 02139, USA
[h] Department of Material Science and Engineering, Hanyang University, Seoul, 04763, South Korea

ARTICLE INFO

Keywords:
Molten salts corrosion
Computational predictions
Thermodynamics
Material protection
Protective coatings

ABSTRACT

Molten salts enable numerous industrial applications, yet trace impurities such as moisture accelerate corrosion despite the salts' chemical stability. Existing phase stability diagrams, often useful for corrosion analyses, disregard such impurities, underscoring the need for an impurity-aware, holistic framework. Here, we present a computational framework for impurity-inclusive phase stability diagrams in molten salts. Using chloride melts as model systems, we demonstrate three-dimensional stability maps with pO^{2-} and pH as the coordinate plane, revealing how moisture and oxygenated species influence the phase stability of structural materials. Applied to 56 Fe-, Cr- or Ni-containing binary systems, these diagrams quantitatively predict that boriding or siliconizing markedly improves the corrosion resistance of Fe and Cr, and provide explicit purification targets for molten chlorides. The predictions are verified with electrochemical characterizations and static corrosion tests. Our results provide a practical guide to designing molten salt-stable materials or synthesis protocols in molten salts.

1. Introduction

Molten salts with high boiling points and chemical stability support a wide range of industrial applications including high-temperature energy storage [1–3], molten salt nuclear reactors with enhanced safety and efficiency [4,5], recycling of rare-earth elements [6–8] or synthesis media for functional ceramics [9–11]. Ensuring reliable performance across these diverse applications demands a thorough understanding of how materials remain stable under molten salt conditions.

Efforts to assess the relative thermodynamic stability in molten salts date back to Littlewood [12] as he developed the first diagrammatic framework for phase stability in molten halides as a function of oxygen ion concentrations (pO^{2-}) [13]. The diagrams were soon conceptually extended to carbonates [14], nitrates [15], and sulfates [16]. With the development of *in situ* pO^{2-} measurement techniques [17] and oxygen electrodes [18], such diagrams helped rationalize silver corrosion in nitrate melts [19], chromium oxide dissolution in humid chloride-sulfate melts [20], or selective dissolution of alloy elements in halide melts [21]. Also, modern experimental techniques and computational tools made progress toward building relevant datasets for metallic stability in molten salts [22].

Yet, several key challenges remain. Most commercial alloys remain susceptible to corrosion in molten chlorides [23]. Only a trace amount of impurities such as moisture has been reported to alter the corrosion rates by orders of magnitudes in molten salts [22,24], and statistical analyses of historical corrosion data in molten chloride and fluoride salts similarly identify salt purity as one of the primary factors governing alloy degradation [25]. Recent electrochemical and *in situ* imaging studies in LiCl-KCl have shown impurity-controlled dealloying and morphology changes in Fe-(Cr)-Ni and Ni-Cr alloys [26,27]. However, the current

* Corresponding authors.
E-mail addresses: liju@mit.edu (J. Li), sangtae@hanyang.ac.kr (S. Kim).
[1] Those authors (S. Ham and C. Kwon) contributed equally to this work.

https://doi.org/10.1016/j.actamat.2026.122063
Received 17 June 2025; Received in revised form 23 February 2026; Accepted 25 February 2026
Available online 26 February 2026

understanding of phase stability via Littlewood diagrams essentially neglects the effect of impurities other than oxygen ions, while the relative phase stability changes with numerous variables including metal ion concentrations or humidity. The phase stability of ceramics in molten salts also remains largely unexplored. Heuristic and trial and error-based approaches employing boronized alloys [28], aluminum oxides [29], or yttria-stabilized zirconia coatings [30] have been reported to improve corrosion-resistance in molten chlorides; however, the detailed thermodynamic understanding of how these coatings remain stable or whether these coatings remain stable against impurities remain largely unanswered. The detailed thermodynamic understanding of phase stability in molten salts with impurities and the systematic design principles for corrosion-resistant alloys or coatings remain elusive. Compounding the limited theoretical understanding, there are also difficulties in high-temperature experimentation [31], severe effects of low-level impurities such as moisture [32], lack of reliable *in situ*

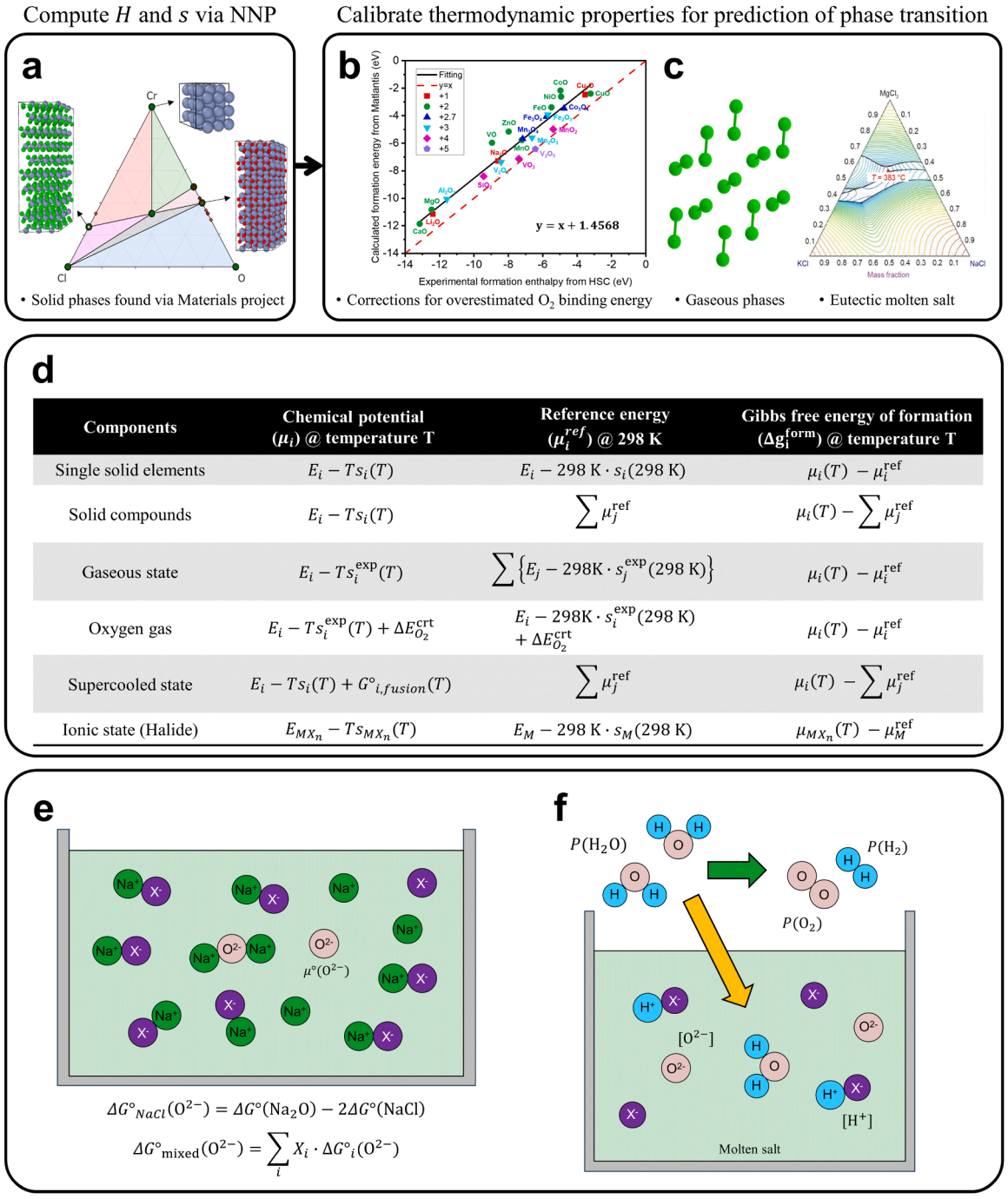

d

Components	Chemical potential (μ_i) @ temperature T	Reference energy (μ_i^{ref}) @ 298 K	Gibbs free energy of formation (Δg_i^{form}) @ temperature T
Single solid elements	$E_i - Ts_i(T)$	$E_i - 298\,\mathrm{K} \cdot s_i(298\,\mathrm{K})$	$\mu_i(T) - \mu_i^{\mathrm{ref}}$
Solid compounds	$E_i - Ts_i(T)$	$\sum \mu_j^{\mathrm{ref}}$	$\mu_i(T) - \sum \mu_j^{\mathrm{ref}}$
Gaseous state	$E_i - Ts_i^{\mathrm{exp}}(T)$	$\sum \left\{E_j - 298\mathrm{K} \cdot s_j^{\mathrm{exp}}(298\,\mathrm{K})\right\}$	$\mu_i(T) - \mu_i^{\mathrm{ref}}$
Oxygen gas	$E_i - Ts_i^{\mathrm{exp}}(T) + \Delta E_{O_2}^{\mathrm{crt}}$	$E_i - 298\mathrm{K} \cdot s_i^{\mathrm{exp}}(298\,\mathrm{K}) + \Delta E_{O_2}^{\mathrm{crt}}$	$\mu_i(T) - \mu_i^{\mathrm{ref}}$
Supercooled state	$E_i - Ts_i(T) + G^{\circ}_{i,fusion}(T)$	$\sum \mu_j^{\mathrm{ref}}$	$\mu_i(T) - \sum \mu_j^{\mathrm{ref}}$
Ionic state (Halide)	$E_{MX_n} - Ts_{MX_n}(T)$	$E_M - 298\,\mathrm{K} \cdot s_M(298\,\mathrm{K})$	$\mu_{MX_n}(T) - \mu_M^{\mathrm{ref}}$

Fig. 1. The schematic for computing the chemical potential and Gibbs free energy of formation for the included phases in the stability diagram (a) The stable or experimentally observed phases in the relevant composition space obtained from phase diagrams (in the figure, Cr-Cl-O system is shown as an example) (b) The oxygen molecule energy correction from non-transition metal oxides (c) The free energies of non-solid phases considered in the framework with energy corrections (d) The table of chemical potential schemes for different chemical species (e) The chemical potential for oxide ion estimated from the oxide formation energies (f) The moisture decomposition schemes and moisture-derived impurities.

characterization methods to probe interfacial phenomena, and the difficulty in accurate predictive modeling due to the limited reliable thermodynamic data for molten salt-solid interactions.

Here, we extend Littlewood diagrams to account for major impurities such as moisture and metal ions, demonstrating three-dimensional phase-stability diagrams for molten chlorides. We rationalize how oxygen- and hydrogen-related species, derived from water decomposition, influence phase stability. Building on these developments, the impurity-inclusive phase-stability diagrams are extended to provide a thermodynamic framework that rationalizes the impurity-dependent corrosion behavior and the coating design principles applied to ceramic coatings and practical engineering alloys.

2. Methods and materials

2.1. Chemical potential computation and Pourbaix diagram construction

The framework to computationally construct molten salt stability diagrams begins with identifying the relevant solid phases in the compositional space using phase diagrams of the M-A-O ternary systems (M indicates Ni, Fe, and Cr, and A indicates anion species) available in the Materials Project (Fig. 1a) [33]. The total energies and vibrational entropies of all listed phases were computed via harmonic approximation and phonon dispersion calculations at 298 K and 1000 K, employing PFP universal neural network interatomic potentials as implemented in Matlantis™software [34,35]. A force convergence criterion of 10^{-4} eV/Å was applied and the crystal_u0 mode in PFP version 6.0.0 was employed for solid phases. The computed total energy was taken as the enthalpy [36], assuming a negligible contribution from volumetric changes. Thermal contributions to entropy were derived from the vibrational density of states. The free energy of each phase at 1000 K was then estimated by adding the entropic contributions from phonon dispersion to the 0 K energy and comparing these values to those of the constituent elements at 1000 K [36].

Several calibration steps were incorporated to construct the stability diagrams. First, an energy correction term was applied to the O_2 chemical potential to account for its overestimated binding energy [37]. Specifically, the computed formation energies of all 23 metal oxides selected from the study by Wang et al. were compared to experimental values at 298 K from the HSC chemistry version 10 (Fig. 1b), and an offset of +1.4568 eV per O_2 molecule was employed. Thermal properties of liquids and gases were also obtained from experimental data available in HSC Chemistry version 10. The Pourbaix diagrams were constructed using the Atomic Simulations Environment (ASE) package with the computed free energies as inputs-similar approaches have been employed for aqueous Pourbaix diagrams via computations [38]. Finally, the chemical potential of ionic phases (e.g., Fe^{2+}in chloride salts) was estimated from the Gibbs free energy of the corresponding salt (e.g., $FeCl_2$) in HSC Chemistry version 10. When pure salts have melting points above 1000 K (e.g. NaCl), supercooled states were assumed by adjusting the energies using the experimentally obtained latent heat of melting from the NIST-JANAF tables in Fig. 1c [39].

Chemical potentials for each species at a given temperature in a specific molten salt were then derived from the computed energies relative to reference energies calibrated at 298 K (Fig. 1d). The 298 K reference reflects the calibration of oxide formation energies and O_2 correction terms. The Gibbs free energy of formation was obtained by subtracting the sum of the reference energies of the components from the chemical potential of the species, which was then input into the code for the Pourbaix-like diagram construction. Additionally, the impurities (e.g. moisture and oxide ions) and their equilibrium redox potentials were incorporated into the phase diagrams (Fig. 1e).

2.2. Sample preparation for coated stainless specimens

Stainless steel 316 L (SS316L), an ASME BPVC-qualified austenitic alloy widely considered for high-temperature molten-salt reactors and thermal-storage systems, was selected as the substrate material. It provides a realistic engineering test case compared to idealized pure Fe or Cr model materials. The stainless steel 316 plates of 7 × 20 × 2 mm for widths, heights, and thicknesses were first polished and pickled in a 5 vol % HF and 45 vol % HNO_3 aqueous solution for 3 min before coating preparation. The plates were cleaned in ethanol using an ultrasonic cleaner. Some samples had a 3 mm diameter hole for partial immersion during corrosion tests. Four types of SS316L specimens were prepared for the molten-salt corrosion study: bare (uncoated), nitrided, siliconized, and yttria-coated. The siliconized coating on SS316 was manufactured by pack cementation. The powder pack consisted of 30 wt % silicon powder (Si, −325 mesh, >99 %, Sigma-Aldrich), 1 wt % sodium fluoride (NaF, >99 %, Sigma-Aldrich) as an activator, and 69 wt % silicon dioxide (SiO_2, >99 %, Sigma-Aldrich) as insert fillers. The powder and a SS316 plate were placed in an alumina crucible (inner diameter: 36 mm, height: 45 mm, wall thickness: 3.5 mm, with a lid) and sealed with high-temperature concrete (Durabond™ 7031) in an Ar environment to prevent potential oxidation or gas leakage. The crucible was heated at 800 °C for 12 hours in an argon-filled gas furnace (R-A1400 mini, Hantech). The nitride coating was obtained by salt bath nitriding at a commercial plant, and the yttria coating was obtained by plasma spray coating.

2.3. Molten salt experiments

The static corrosion tests were performed at an elevated temperature of 800 °C for accelerated corrosion tests using a salt mixture composed of 50 wt % KCl (>99 %, Sigma-Aldrich) and 50 wt % NaCl (>99 %, Sigma-Aldrich). The salts were selected for their wide use as a chemically neutral chloride matrix for static corrosion evaluation of stainless steels and Ni-based alloys [40]. For tests involving $MgCl_2$-containing melts, we used anhydrous $MgCl_2$ (>99 %, Yakuri Pure Chemicals Co., Ltd.) and prepared a 50.5 mol % KCl-46.6 mol % $MgCl_2$–2.9 mol % NaCl mixture following D'Souza et al. [28].. These $MgCl_2$-containing static corrosion tests were performed only on bare and siliconized SS316L specimens to probe the effect of salt composition on an unprotected and a siliconized surface. All salts were handled and blended in an Ar-filled glovebox and thermally dried at 600°C for 48 h using the same protocol, then stored under Ar until used for the $MgCl_2$-containing experiments reported in the Supplementary Information. The salts were placed in an alumina crucible and thermally refined at 600 °C for 48 hours in an Ar-filled glove box. The corrosion test was conducted at 800 °C for 100 hours by completely immersing each coated and uncoated specimen in a separate salt-containing alumina crucible with a lid. The salt amount was ensured to exceed the salt volume-to-specimen surface area ratio of 0.4 mL/mm^2. After the corrosion test, the specimens were rinsed first with ethanol and then with deionized water in an ultrasonic cleaner to remove residual salt from the surface. The corroded surface and the cross-section were analyzed using scanning electron microscope (SEM)-EDS to assess the corrosion depth and any selective dissolution of specific metallic elements.

The electrochemical characterization and measurements on bare, nitrided, siliconized, and yttria-coated SS316L specimens were conducted using approximately 10 g of eutectic LiCl-KCl salt mixture (99.99 %, AnhydroBeads™, Sigma-Aldrich) at 500 °C. The eutectic salts were selected for testing at a lowered temperature to ensure the sensor and reference electrode stability [41,42]. This eutectic composition was chosen because the Ag/AgCl reference electrode used in this work was calibrated in LiCl-KCl, which enables accurate conversion of the measured potentials to the Cl_2/Cl^- scale. A quartz cylinder tube with an outer diameter of 30 mm and a thickness of 1.5 mm, with one end finished in a hemispherical shape, was used to contain the molten salt. A Biologic SP-240 potentiostat was used for the open circuit potential, Tafel, cyclic voltammetry, and potentiostatic polarization measurements. A Ni wire (99.99 %, Nilaco) with a diameter of 0.5 mm was used

to connect the specimen, which served as the working electrode, to the potentiostat. In this setup, the Ni wire was not immersed in the molten salt, ensuring that it did not cause any electrochemical interference. A tungsten rod (99.95 %, Nilaco) with a diameter of 1.5 mm was used as the counter electrode. The reference electrode was an assembly consisting of a 1 mm Ag wire (>99.9 %, Nilaco) and a mixed salt containing 1 wt % AgCl in LiCl-KCl, enclosed within a borosilicate glass tube. The measured potentials were converted from the Ag/AgCl reference (1 wt. % AgCl) to the Cl_2/Cl^- scale by applying a constant offset of −1.210 V, based on three-electrode calibration data obtained under the same LiCl-KCl conditions and consistent with independent Ag/AgCl to Cl_2/Cl^- determinations in the literature [43–45]. Furthermore, this empirical offset is theoretically consistent with the activity of AgCl dissolved in the melt; using the activity coefficient ($\gamma_{AgCl} = 2.516$) reported by Zhang et al. [45]. for 1 wt. % AgCl, the calculated activity ($a_{AgCl} \approx 9.8 \times 10^{-3}$) closely matches the measured potential difference. Unless otherwise noted, all electrochemical potentials in this work are reported versus Cl_2/Cl^- scale using this empirical calibration, with the Cl_2/Cl^- couple serving as a convenient reference zero for the potential scale rather than as a controlled equilibrium state in the experiments.

After partially immersing the specimen in the molten salt, the immersion state was recorded through the quartz crystal window attached to the electrical furnace to monitor whether the experiment was conducted properly under the planned conditions. Before initiating all experiments, the specimen was gently re-immersed to remove any remaining bubbles on the surface (Supplementary Fig. 1a). The open circuit potentials were measured for 30 min. The scan rate of 1 mV/s was set for the Tafel plot and that of 100 mV/s for cyclic voltammetry. The surface areas of the immersed specimens were obtained by measuring the trapezoid area of the front and back surfaces after the corrosion experiments (Supplementary Fig. 1b). The surface area of the roughened siliconized specimen was obtained using a confocal laser scanning microscope (Supplementary Fig. 1c).

All static corrosion and electrochemical experiments were conducted using high-purity alumina crucibles. Although recent studies have suggested that alumina crucibles may act as an oxide-ion source in U-containing molten chlorides [46], previous corrosion and electrochemical studies performed in alkali chloride melts without uranium chlorides have consistently reported alumina to be chemically inert, with no observable crucible degradation or crucible-derived oxide film formation on alloy surfaces. In the present work, no significant oxide phases were detected on the coated specimens after corrosion tests, as confirmed by SEM-EDS and XRD analyses (Supplementary Fig. 13). On this basis, alumina crucibles were considered to be effectively inert under the present experimental conditions, namely NaCl-KCl or LiCl-KCl melts without UCl_x.

3. Result and discussion

3.1. Framework for phase stability assessment

A modeled molten salt electrochemical system with ceramic working electrode is illustrated in Fig. 2a. Since the salt constituent ions are electrochemically stable, the primary interactions originate from three major impurities, namely hydrogen ions (H^+) from moisture hydrolysis, dissolved oxygen species (O_2 or O^{2-}) or corroded metal ions (M^{n+}). H^+ ions promote oxidation by being reduced to H_2, while O_2 or O^{2-} oxidizes solids ($MO_{\frac{n}{2}}$ and $AO_{\frac{m}{2}}$) or dissolves oxides by forming oxyanion species. That is to say, we expect the HCl/H_2 and O_2/O^{2-} equilibria and the metal/dissolved metal ion equilibria are expected to govern the primary corrosion in chloride melts with these impurities. We also assume that the chlorine activity is low enough that Cl_2 does not directly control corrosion reactions; this justifies the electrode potential referenced to the standard Cl_2/Cl^- couple as the conventional Littlewood diagrams do. The standard Cl_2/Cl^- couple is used only to define the zero of the potential axes.

In this picture, the Littlewood diagram can be extended into multi-dimensions, incorporating the above-mentioned impurities and potentially other variables affecting the chemical potentials as individual axes (Fig. 2b). In this work, we demonstrate three-dimensional derivatives with two of the three above-mentioned impurities as the coordinate plane. An illustrative example of Fe in molten LiCl at 1000 K is shown in Fig. 2c, with pO^{2-} and $[Fe^{n+}]$ as the base axes. At low $[Fe^{n+}]$, Fe exhibits no passivity and corrodes into either Fe^{2+} or FeO_2^-, depending on pO^{2-}. With increased $[Fe^{n+}]$, regions with iron oxides appear as the equilibrium shifts towards reduced $[Fe^{n+}]$. The decreased tendency to corrode at increased $[Fe^{n+}]$, as evidenced by the increasing corrosion potential for Fe/Fe^{2+}boundary, suggests that corrosion may be self-slowing after extended corrosion and that sufficient volume of molten salts is required for accurate corrosion assessment [47]. Also, the solubility of iron oxides increases with both increasing or decreasing pO^{2-} from $pO^{2-} \approx 10$, similar to experimentally observed iron oxide solubility [20].

Employing the typical Pourbaix formalism with fixed metal ion concentrations of 10^{-6} M and gaseous partial pressures of 10^{-6} atm, we construct a three-dimensional phase-stability diagram for the Fe/FeB system in LiCl at 1000 K with pH, pO^{2-}, and the electrode potential (E) as the axes (Fig. 3a). This 3D diagram is obtained by first computing a series of two-dimensional phase-stability diagrams at fixed pO^{2-} or fixed pH and then combining these slices. All of the diagrams in Fig. 3 are

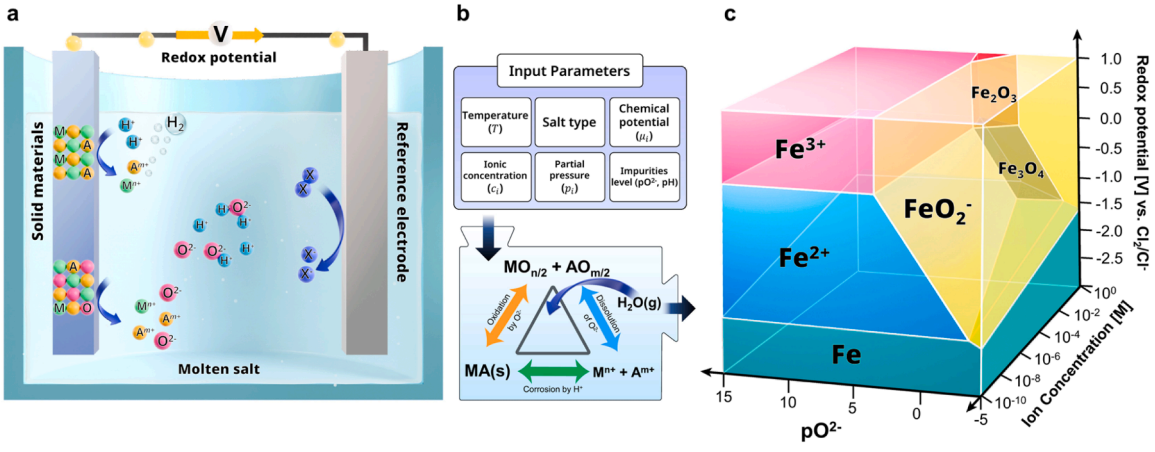

Fig. 2. The framework for the molten salt stability diagram. (a) Schematic of a model molten salt system and the major impurity-driven corrosion mechanisms (b) The input parameter sets and the reactions considered for phase stability in molten salts (c) The constructed phase stability diagram for Fe in molten LiCl at 1000 K with pO^{2-} and ion concentrations as the coordinate plane.

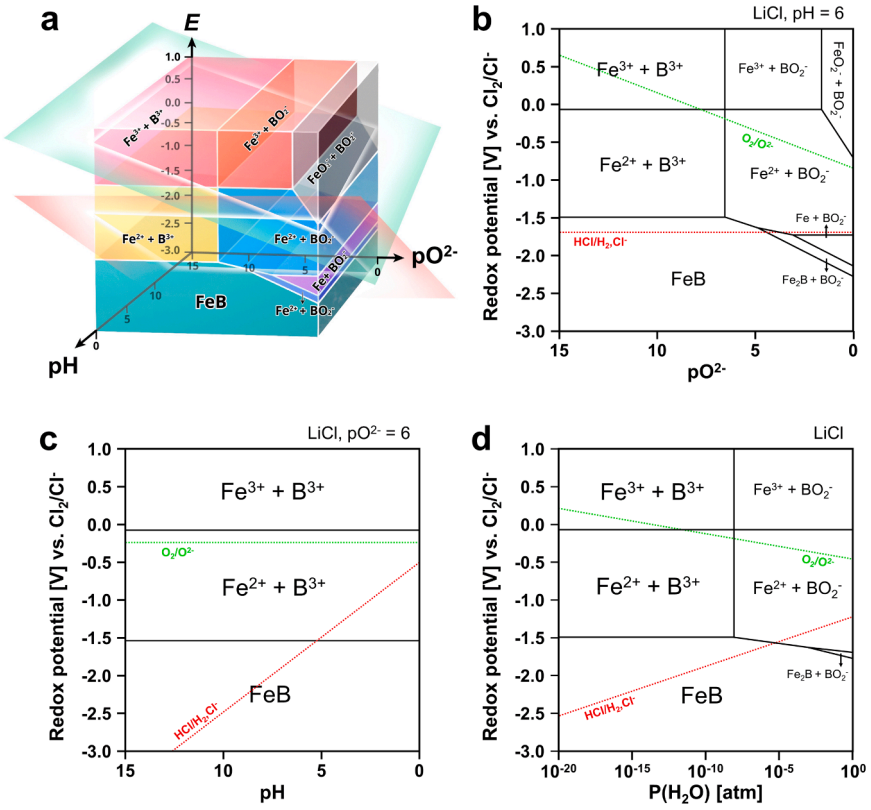

Fig. 3. Phase stability diagrams for iron borides along with impurities' redox potentials. (a) The constructed 3D phase stability diagram with pH, pO^{2-} and *E* axes at 1000 K in LiCl. The equilibrium redox potentials for impurities are drawn as green (O_2/O^{2-}) and red (HCl/H_2) planes intersecting the 3D diagram. (b) The *E*-pO^{2-} diagram obtained by slicing the 3D diagram at pH = 6 and (c) the *E*-pH diagram by slicing at pO^{2-} =6. (d) The *E*-*P*(H_2O) diagram obtained by slicing along a fixed line $[H^+]:[O^{2-}]=2:1$.

generated from the same underlying thermodynamic dataset. It is possible to section the three-dimensional diagram into *E*-pO^{2-} planes at a given pH (essentially the Littlewood diagram) or *E*-pH planes at a given pO^{2-} (Figs. 3b-c). These cross-sections provide a readable view of the phase boundaries. The quantitative stability thresholds are discussed in terms of these cross-sections throughout Section 3.1.

In these diagrams, the equilibrium potentials of O_2/O^{2-} and HCl/H_2 are shown as green and red planes, respectively. Regions above the green plane involves oxygen gas evolution from oxidation of oxide ions and thus are not considered in detail. Regions below the red plane reduce HCl into H_2 gas, accompanying oxidation of solids if its redox potential lies below this plane. Bare iron has the redox potential just below the red plane, with active corrosion expected in this potential regime. Forming Fe_2B pushes the redox potential above the red plane at pO^{2-} below 3.78, improving corrosion resistance. In this sense, the redox potential gap between HCl/H_2 and a solid phase quantifies the corrosion tendency of the solid phase. Similarly, the red dotted line in the *E*-pH diagram crosses the FeB/Fe^{2+} phase boundary at pH = 5.25; when $[H^+]$ exceeds this threshold, FeB is expected to corrode. *E*-pO^{2-} diagrams show the stable phase boundaries and oxide stability, while they do not capture the effects of H^+ on corrosion as pH remains fixed. In contrast, the *E*-pH diagram effectively captures the HCl/H_2 redox potential as a function of pH, yet is ill-suited for assessing the phase stability except for the unlikely hydrides in molten salts at a fixed pO^{2-}. Essentially a three-dimensional construct is required to examine the comprehensive corrosion behavior by moisture. Also, if moisture is the sole source of $[H^+]$ and $[O^{2-}]$, sectioning the three-dimensional diagram along the line for $[H^+]:[O^{2-}]=2:1$ allows for assessing the effect of moisture partial pressure ($P(H_2O)$) on the phase stability (Fig. 3d). The red plane intersects the FeB/Fe^{2+} boundary at $10^{-5.30}$ atm H_2O. A more general approach is possible with equilibrium constants for water dissociation, and the obtained critical moisture or impurity contents for corrosion analyses may serve as guidelines for salt purification that suppresses corrosion.

While this equilibrium framework provides clear baselines for sealed and static environments, its applicability to open or flowing molten-salt systems warrants further discussion. In practical flowing systems comprising a hot leg and a cold leg, temperature gradients inevitably induce spatial variations in local redox conditions and mass transport. Within such dynamic environments, our framework is best interpreted as a local thermodynamic map: once the local temperature and effective redox state at a specific location are specified, it can evaluate the local equilibrium phase assemblage and corrosion driving forces. However, a fully quantitative prediction of system-level degradation would require coupling this equilibrium framework with transport-reaction models. Furthermore, in open systems where the salt interacts with reactive atmospheres, the effective Cl_2/Cl^- equilibrium can drift over time, potentially shifting the corrosion mechanism away from the ion-dissolution pathways assumed in this static framework. Therefore, it is necessary to extend this static framework to encompass spatially varying redox gradients in flowing loops and shifting redox equilibria in open systems.

3.2. *Effects of impurities according to the salt type*

Adopting Littlewood's method, we first compute the formation energy of oxide ions ($\Delta G_f(O^{2-})$) and chemical potential ($\mu(O^{2-})$) in individual chloride salts [12]. The choice of salt type alters the oxide ion chemical potential, influencing both phase boundaries and impurity redox planes. In practice, the oxide ion chemical potentials are computed from the oxidation reactions of the metallic species present in the salt constituents [22], and the chemical potentials of oxide ions at

1000 K for various salts are provided in Table 1. The phase boundaries in E-pO^{2-} and E-pH diagrams shift in the pO^{2-} or pH direction as $\mu(O^{2-})$ varies across different salts. Although the relative positions of phase boundaries with respect to impurity redox lines do not readily change, the critical pO^{2-} or pH levels for corrosion shift horizontally among chloride salts in an order similar to oxide stability ($MgO>CaO>Li_2O>Na_2O>K_2O$) (Supplementary Figs. 2–3).

Changes in $\mu(O^{2-})$ also lead to variations in impurity concentrations derived from moisture under identical $P(H_2O)$ condition. The relationship among equilibrium pO^{2-}, pH and $P(H_2O)$ follows from the equilibrium of H_2O dissolution in molten chlorides, as expressed in Eqs. (1) and (2), where ΔG° stands for the free energy of H_2O dissolution at the salt temperature.

$$H_2O(g) + 2X^- \leftrightarrow 2HX + O^{2-} \quad (1)$$

$$\log P(H_2O) + 2pH + pO^{2-} = \frac{\Delta G^{\circ}}{RT\ln 10} \quad (2)$$

At a fixed pH of 6 (or pO^{2-} of 6) and the moisture vapor pressure of 10^{-6} atm (a typical value for glovebox-controlled atmosphere), the equilibrium concentration of pO^{2-} (or pH) derived from moisture are shown in Supplementary Table 1. These pO^{2-} and pH values are shown as gray dotted lines in the E-pO^{2-} (Supplementary Fig. 2) and the E-pH (Supplementary Fig. 3) diagrams.

To simplify the analyses on impurity effects, we next assume that moisture is the sole source of $[H^+]$ and $[O^{2-}]$ (fixed at $[H^+]:[O^{2-}] = 2:1$) and present the data in Table 2 and Fig. 4. Table 2 summarizes the equilibrium $[H^+]$ and $[O^{2-}]$ concentrations at 1000 K in each chloride melt for $P(H_2O) = 10^{-6}$ atm, obtained by combining the oxide-ion chemical potentials in Table 1 with the water-dissolution equilibria in Eq. (1). These values show that, even at the same moisture level, the dissolved impurity concentrations span several orders of magnitude depending on the chloride salt. Using the same dissolution equilibria, we then convert each $P(H_2O)$ level into the corresponding impurity redox potentials and plot them on the E-$P(H_2O)$ diagrams in Fig. 4 to evaluate the redox-potential gap and the associated corrosion thresholds.

To compare the corrosion driving force among different salts, we first focus on $P(H_2O) = 10^{-6}$ atm (the gray line in Figs. 4a-e), which is representative of a typical well-controlled moisture environment such as a glovebox. At this moisture level, the redox potential gap between the oxidation boundary for Fe (or FeB_x) and the HCl/H_2 equilibrium redox potential shows that the redox potential gap of −0.479 V for $MgCl_2$, −0.026 V for $CaCl_2$, +0.050 V for LiCl, +0.432 V for NaCl, and +0.792 V for KCl. A negative redox potential gap indicates spontaneous corrosion or oxidation, whereas a positive gap indicates a non-spontaneous reaction at $P(H_2O) = 10^{-6}$ atm. We then use the E-$P(H_2O)$ diagrams in Figs. 4a-e to determine, for each salt, the moisture pressure at which the HCl/H_2 redox potential just intersects the Fe (or FeB_x) oxidation boundary. These threshold $P(H_2O)$ values are summarized in Fig. 4f, showing that $MgCl_2$ requires moisture pressure below $10^{-13.22}$ atm to suppress HCl-driven corrosion of FeB, whereas for NaCl and KCl, this threshold increases to $10^{0.53}$ and $10^{-0.56}$ atm, respectively.

Although KCl has the least-stable oxide ion (largest $\mu(O^{2-})$) among the chlorides considered, the NaCl melt exhibits a slightly higher $P(H_2O)$ threshold than KCl in our framework. This apparently counterintuitive ordering can be rationalized in terms of oxo-acidity. In the more oxo-basic KCl melt, the elevated chemical potential of O^{2-} promotes further oxidation of iron to higher-valence oxyanionic species (e.g., FeO_2^-, FeO_4^{5-}) at increased pO^{2-}, leading to corrosion that is dominated by the formation of FeO_4^{5-} rather than dissolution as Fe^{2+}. As a result, the effective stability fields of Fe/FeB_x plus oxyanion phases are shifted to more positive potentials relative to the HCl/H_2 line, and the intersection with this redox boundary occurs at a lower $P(H_2O)$ in KCl than in NaCl. These results quantitatively demonstrate that impurity concentration strongly depends on the salt type and that the corrosion behavior (phase stability) varies with salt composition, even under the same $P(H_2O)$ level. Therefore, we use equilibrium $P(H_2O)$ values as a reference to compare the effects of impurities on phase transitions and salt purification criteria in different molten chlorides. This aligns well with highly corrosive $MgCl_2$ salts, although the model does not fully consider the hydroxides and oxychlorides present in $MgCl_2$-based melts [48].

Table 1
The chemical potential of O^{2-} in various chloride melts at 1000 K.

Chloride salt	$MgCl_2$	$CaCl_2$	LiCl	NaCl	KCl
$\mu(O^{2-})$	−1.6339 eV	−0.2764 eV	0.1344 eV	1.8070 eV	2.8872 eV

Table 2
The equilibrium $[O^{2-}]$ and $[H^+]$ concentrations in various molten chlorides at 1000 K under $P(H_2O) = 10^{-6}$ atm, assuming that the ions originate only from moisture and maintain the fixed ratio of $[H^+]:[O^{2-}] = 2:1$.

Chloride salt	$MgCl_2$	$CaCl_2$	LiCl	NaCl	KCl
$[O^{2-}]$	$10^{-2.605}$ M	$10^{-4.886}$ M	$10^{-5.576}$ M	$10^{-8.386}$ M	$10^{-10.200}$ M
$[H^+]$	$10^{-2.906}$ M	$10^{-5.187}$ M	$10^{-5.877}$ M	$10^{-8.687}$ M	$10^{-10.501}$ M

3.3. Design of corrosion-resistant coatings

Building on the impurity-dependent stability diagrams developed in Sections 3.1 and 3.2, we use the constructed phase stability diagrams to aid in designing corrosion-resistant ceramic coatings for Cr-containing alloys, as Cr has the lowest redox potential among Cr, Fe, and Ni [22]. Fig.s 5a-c present the constructed E-pO^{2-} diagrams at a fixed moisture content of 10^{-6} atm for bare Cr, CrB, and CrSi. The redox potential of Cr lies 0.32 V below that of HCl/H_2, indicating a strong tendency toward Cr dissolution. Cr_2O_3 does not appear in the diagram, indicating active dissolution into oxoanions at elevated pO^{2-}andlow metal ion concentrations. Upon forming CrB, the equilibrium potential for partial CrB dissolution into Cr^{2+} andBO_2^- rises by 0.01 V above the HCl/H_2 equilibrium potential, indicating a notably reduced corrosion tendency. The observation is consistent with the experimentally measured corrosion resistance of boronized Cr-containing alloys [28]. The solid-phase boundary intersects the HCl/H_2 line corresponding to CrB/Cr^{2+} at $pO^{2-} = 4.90$, equivalent to $10^{-5.87}$ atm of moisture partial pressure. The corrosion potential of this phase boundary (corrosion potential) decreases as pO^{2-} increases. In other words, if the oxide ion concentration remains below $10^{-4.90}$ M, CrB remains resistant to corrosion under these environmental conditions. Similarly, the equilibrium potential for $CrSi_2$ lies 0.06 V above that of HCl/H_2 line at $pO^{2-} > 4.98$, thereby enhancing corrosion resistance compared to bare Cr [28]. However, at higher pO^{2-} condition, the E-pO^{2-} diagrams in Figs. 5b-c show that the redox potential of the CrB/Cr^{2+} phase boundary eventually exceeds that of $CrSi_2/Cr^{2+}$, so borides become the more noble and corrosion-resistant phase. This behavior reflects the different oxo-acid characteristics of B and Si in chloride melts: BO_2^- becomes thermodynamically stable already at relatively low pO^{2-}, which promotes the decomposition of CrB into dissolved Cr^{2+}/Cr^{3+} and BO_2^- even when only modest amounts of O^{2-} are present, whereas SiO_3^{2-} is stabilized only under strongly oxidizing (high pO^{2-}) conditions. As a result, for $P(H_2O) = 10^{-6}$ atm, which is typical of glovebox-controlled conditions, chromium silicide remains stable over a wider pO^{2-} window than chromium boride and is therefore predicted to provide better corrosion resistance in chloride melts that are purified but not extremely dried (i.e., around $P(H_2O) \approx 10^{-6}$ atm). In contrast, borides are favored in more reducing, low moisture environments. Phosphides, arsenides, and antimonides of Cr and Fe are not thermally stable at 1000 K, and therefore provide no protection against Cr corrosion. The formation of chromium carbide, nitride, or germanide compounds slightly increases the redox potential at the phase boundary between each ceramic compounds and chromium ions. However, this effect is

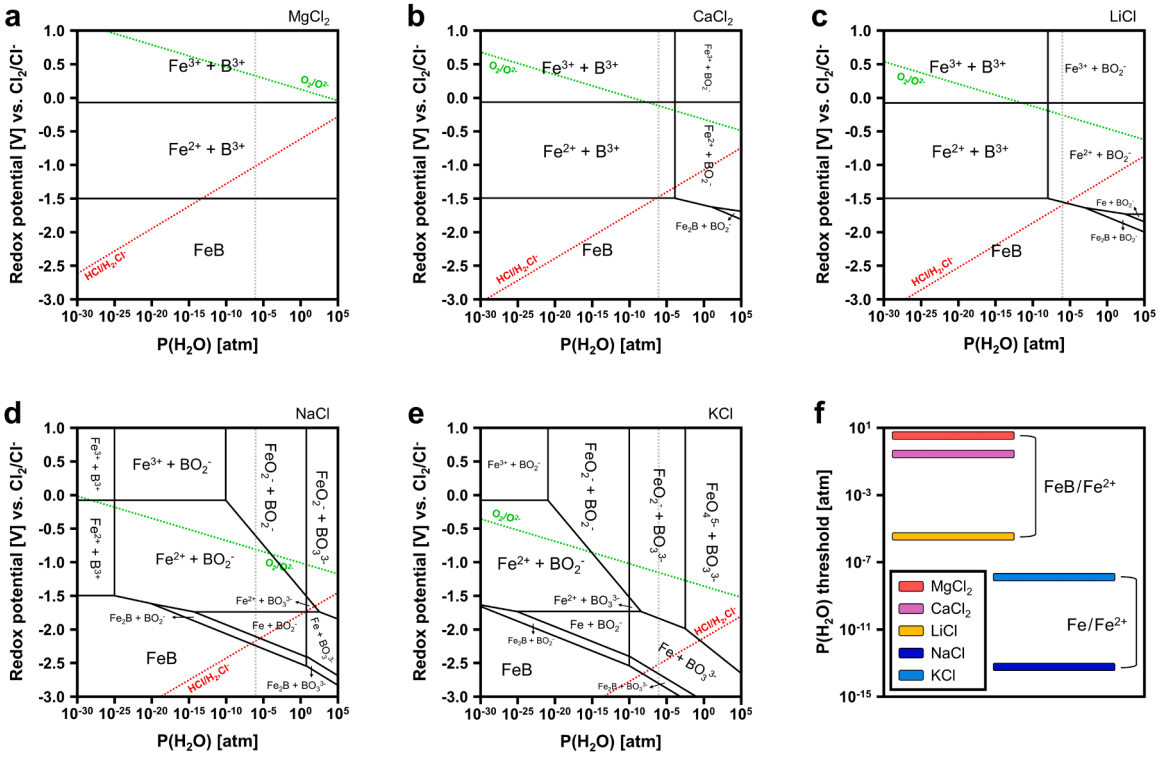

Fig. 4. The *E*-P(H_2O) diagrams for the Fe-B-O ternary system showing impurity redox potential in molten (a) $MgCl_2$, (b) $CaCl_2$, (c) LiCl, (d) NaCl, and (e) KCl at 1000 K, and (f) a design plot summarizing the P(H_2O) threshold required to prevent corrosion in each molten chloride. The concentrations of ionic species are fixed at 10^{-6} M, and the partial pressures of gaseous phases were also fixed as 10^{-6} atm.

insignificant, and the phase boundary remains below HCl reduction line. Notably, nitrides hurt the corrosion resistance because N^{3-} ions form at lower potentials than Cr^{2+}(Supplementary Fig. 4) [49].

Similarly, in iron-based ternary systems, carbon, nitrogen, arsenic, and antimony do not form binary compounds with iron; their corrosion potentials are identical to that of pure Fe (−1.732 V), which positioned below the HCl reduction line (Supplementary Fig. 5). Although the iron phosphide system contains a stable Fe_3P phase, its stability is restricted to low redox potential regions. Fe_3P begins to decompose into pure Fe and P^{3+} ions at redox potentials below the Fe/Fe^{2+} phase transition, resulting in corrosion resistance identical to that of pure Fe metal. In contrast, boron, silicon, and germanium form binary compounds with Fe, enhancing its corrosion resistance against molten chlorides. In the Fe-B-O ternary system, the corrosion potentials of Fe_2B and FeB phases exceed the HCl reduction line at $pO^{2-} > 3.79$ and $pO^{2-} > 4.43$, respectively. The maximum corrosion potential of FeB is −1.496 V. For the iron silicides, the corrosion potential of Fe_3Si and FeSi exceed the HCl reduction line at $pO^{2-} > 3.14$ and $pO^{2-} > 3.41$, respectively; FeSi possesses a maximum corrosion potential of −1.524 V. Similarly, in the iron germanide system, the FeGe phase remains resistant to corrosion over the pO^{2-} range relevant to P(H_2O) = 10^{-6} atm in our diagrams, and the maximum corrosion potential of FeGe is −1.636 V. Among those considered, iron silicides exhibit the highest corrosion potentials at P(H_2O) = 10^{-6} atm, and thus the best predicted corrosion resistance, followed by iron borides and FeGe. Under strongly reducing, low moisture conditions, however, the iron borides recover the broadest stability fields and become the preferred Fe-based ceramic phase.

Nickel exhibits higher corrosion resistance against chlorides than any Cr- or Fe-based ceramic, making it a suitable base element for structural alloys in molten chloride environments (Supplementary Fig. 6). The corrosion potential of pure nickel metal is −1.404 V, which is clearly higher than the HCl reduction potential. Carbon, nitrogen, and arsenic do not form binary compounds with nickel, and nickel phosphide fails to provide protection because it decomposes into P^{3+} ions. Ni-based boride, silicide, germanide, and antimonide compounds also exhibit enhanced corrosion resistance in molten chlorides. However, the increase in corrosion potential due to compound formation is less significant for nickel compared to chromium and iron. Among these systems, only antimony increases the corrosion potential by more than +0.1 V.

Examining eight different anion species on Cr, Fe, or Ni and plotting the equilibrium potentials at pO^{2-}≈5.03 (equivalent to $P(H_2O)$=10^{-6} atm at pH=6) reveals that borides and silicides increase the equilibrium potentials the most for Cr and Fe, while antimony shows the most enhancement for nickel as shown in Fig. 5d In terms of the critical moisture pressures at which the HCl/H_2 redox potential line crosses the solid border as shown in Fig. 3d, similar trends are observed among the anions considered (Supplementary Fig. 7). Forming silicides or borides increases the moisture level at which HCl-driven corrosion stops by over two orders of magnitudes for Cr, pushing the critical moisture level to practical ranges. When similar analyses are applied to intermetallics containing Cr, Fe, or Ni, along with 10 other common metallic elements, the intermetallics exhibit little effect on the corrosion potential for Cr (Supplementary Fig. 8). The chemical systems that ensure equilibrium potential higher than that of HCl/H_2 include Cr-B, Cr-Si, Fe-B, Fe-Si, Fe-Ge and all nickel-based ceramics.

3.4. *Experimental verification of coatings*

To connect the theoretical framework to practical engineering alloys and to experimentally validate the coating-design principles, we prepare stainless steel 316 L (SS) specimens with bare, nitrided, siliconized and yttria-coated surfaces (Supplementary Fig. 9). As noted in Section 2.2, SS316L is an ASME BPVC-qualified austenitic alloy widely considered for high-temperature molten-salt systems, so using coated SS316L rather than pure Fe or Cr allows us to assess how the proposed coatings behave on a structurally relevant substrate. Yttria is selected as an inert coating [50] that does not readily interact with SS, nitride as potentially harmful

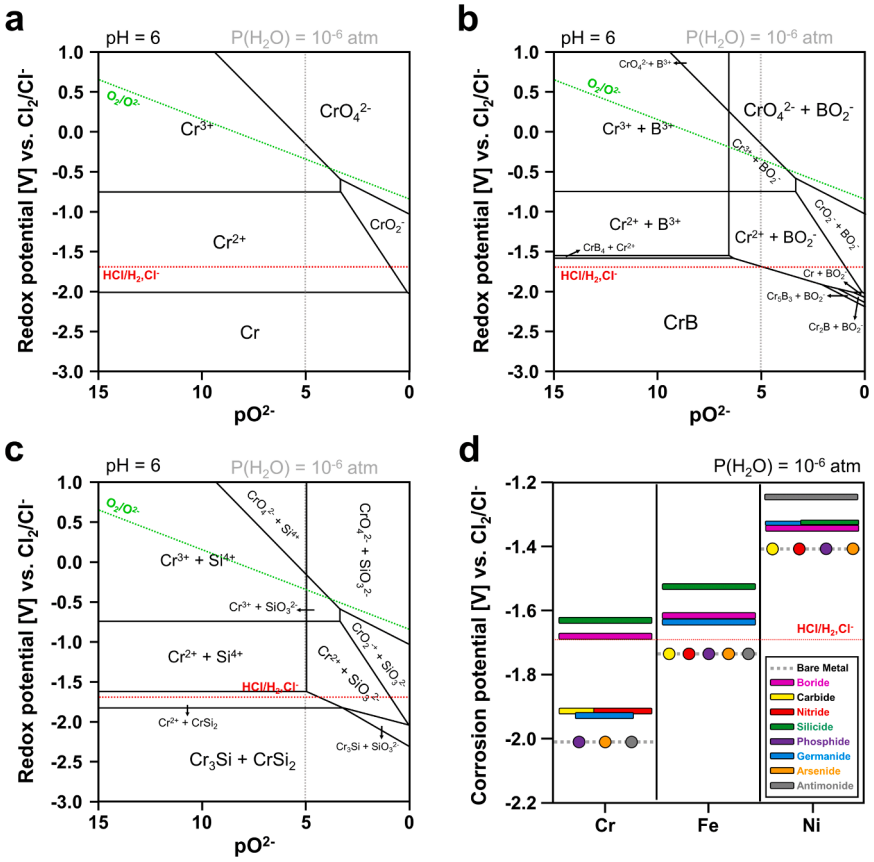

Fig. 5. Stability diagrams for Cr-based ceramics for corrosion resistant coating design. E-pO^{2-} diagrams of (a) bare chromium metal, (b) chromium borides, and (c) chromium silicides at 1000 K in LiCl at the fixed moisture partial pressure of 10^{-6} atm. (d) A design plot showing the corrosion potential of ceramics based on Cr, Fe, and Ni metals and 8 different anion species at pO^{2-} of 5.03 (equivalent to $P(H_2O)=10^{-6}$ atm at pH=6). The red dotted line indicates the HCl/H_2 redox potential.

coating due to nitrogen's electrochemical activity in molten chlorides (Supplementary Fig. 4d and [49]), and silicides as corrosion-resistant coating according to the computed results in Fig. 5. Although our calculations indicate that Cr-, Fe-, and Ni-borides also offer very high thermodynamic stability and corrosion resistance, we do not include a boride-coated specimen because available boronizing routes (e.g. D'souza et al. [28].) rely on proprietary processing that we cannot faithfully reproduce in our facilities; instead, we focus on a siliconized layer whose non-proprietary pack-cementation process is readily implemented in our laboratory. The samples are both electrochemically characterized (followed by potentiostatic polarization) and statically corroded to confirm the predicted corrosion resistance. The Tafel measurements show the lowest corrosion current density for siliconized specimens, followed by yttria-coated, bare, and nitrided specimens (Fig. 6a). The slopes of the anodic Tafel curves are notably decreased for siliconized and yttria-coated specimens, compared to bare and nitrided ones. The corrosion potentials of siliconized specimens from Tafel measurements are shifted to a more negative region by 0.17 V,

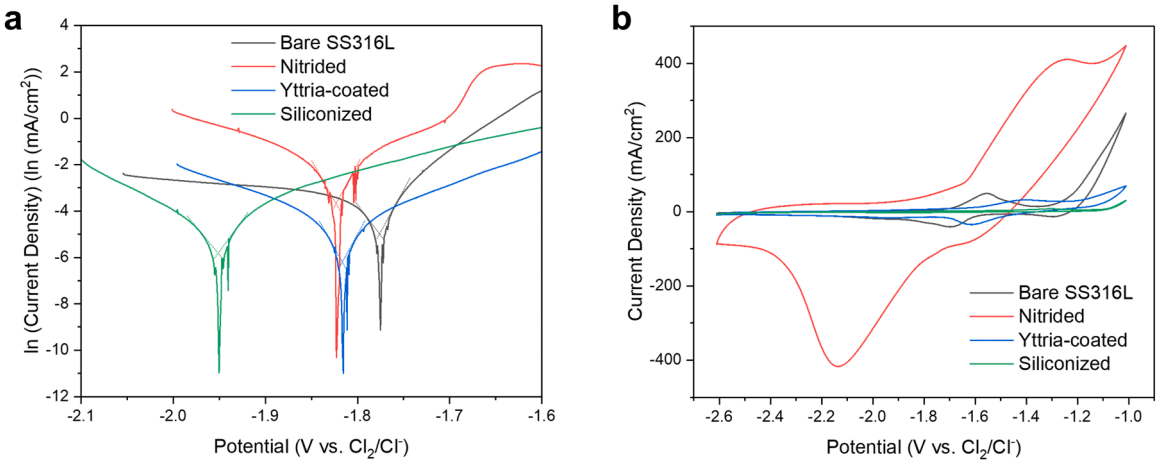

Fig. 6. Electrochemically characterized corrosion resistance of ceramic coatings on SS316L. (a) Tafel plots showing reduced corrosion current and corrosion potentials for siliconized SS316L compared to bare, yttria-coated or nitride specimens (b) The cyclic voltammetry scanned at 100 mV/s showing enhanced corrosion resistance of siliconized SS316L compared to bare, yttria-coated or nitride specimens.

indicating potentially different electrochemical interfaces formed compared to SS316L. Reduced corrosion potentials due to modified electrochemical interfaces despite significantly reduced corrosion rates have also been reported for corrosion-resistant high-entropy coatings [51]. Repeated Tafel measurements show stable corrosion potentials for bare SS316L and siliconized specimens, compared to unstable corrosion potentials for nitride and yttria-coated specimens (Supplementary Fig. 10).

The cyclic voltammetry scanned from the open circuit potential (around −1.75 V vs. Cl_2/Cl^-, Supplementary Fig. 11) to highly oxidizing conditions at −0.9 V and reducing conditions at −2.7 V show a similar corrosion trend, with the lowest redox activity for the siliconized specimen, followed by bare SS316L, yttria-coated specimens and nitrided specimens (Fig. 6b). The measured currents in the reduction directions for bare SS316L show a peak around −1.55 V, close to the reported values for Fe^{2+}/Fe [52]. Post-experimental energy dispersive spectroscopy (EDS) results also confirm Fe dissolution (Supplementary Fig. 12), while the statically corroded SS316L shows Cr-depleted surfaces and grain boundaries (Supplementary Fig. 13). Nitrides exhibit significantly increased redox activity. The reduction peaks near −1.65 V, −2.05 V, and below −2.7 V indicate corroded species of Fe^{2+}, $Cr^{2+,}$ and N^{3-}, respectively [49,52]. The cross-section image of the nitrided sample under static corrosion shows the incomplete coverage of CrN and severe corrosion in the interior, with Cr, Fe and Ni corroded in the nitride region (Supplementary Fig. 14). Yttria-coated specimens exhibit partially broken regions and two major reduction peaks with increased currents for Cr^{2+} and Fe^{2+}, indicating that inert coatings may involve expediated localized corrosion on broken regions (Fig. 6b). Yttria coating forms a relatively continuous layer, whereas the nitride and siliconized coatings contain localized thickness variations and regions with incomplete coverage (Supplementary Fig. 9). Such non-uniform areas can locally expose the stainless-steel substrate and generate small anodic sites surrounded by more noble coated regions, giving rise to micro-galvanic cells. These micro-galvanic couples promote pit-like initiation at the exposed sites and lead to transient increases in local anodic current, which manifest as drift and negative spikes in the open-circuit potential as well as increased noise and run-to-run scatter in the Tafel plots for the nitride- and yttria-coated specimens (Supplementary Fig. 10). For instance, the corrosion potential of the yttria-coated specimen tends to decrease during repeated measurements, which can be attributed to progressive micro-damage increasing the fraction of the exposed active substrate. Conversely, the nitrided specimen exhibits an increasing corrosion potential, likely driven by the preferential dissolution of the more active nitride phase and subsequent cathodic depolarization by accumulating metal ions in the melt. In this sense, the non-uniformity of the coatings primarily affects the detailed electrochemical response (e.g., E_{corr} fluctuations and current noise) but does not alter the overall ranking of corrosion resistance, which is governed by the intrinsic phase stability and the ability of the coating to maintain an effectively continuous barrier under molten-salt conditions.

The electrochemically polarized yttria specimen shows Cr-depleted surfaces beneath broken yttria coating (Supplementary Fig. 15), while the statically corroded specimen shows corrosion stability under 100 hr tests (Supplementary Fig. 16). Siliconized specimens exhibit a wide electrochemical window until −1.1 V with minimal redox activities. A minimal reduction peak for Cr^{2+} is observed around −1.9 V while the oxidation peak is at −1.3 V, indicating significant overpotential for Cr oxidation and minimized Fe corrosion by siliconizing. The corroded siliconized samples both electrochemically and statically show a robust siliconized layer with partial oxides, after minimal corrosion (Supplementary Figs. 17–18). When the static corrosion tests were repeated with molten salts containing $MgCl_2$, bare specimens exhibit increased corrosion depths (Supplementary Figs. 19–20) while siliconized specimens exhibit robust coated surfaces (Supplementary Figs. 21–22). Yet, we also observe Mg incorporated into siliconized layers, indicating the need for intricate coating designs with respect to the salt composition. The potentiostatic polarization at −1.35 V (approximately the potentials for $U^{4+/3+}$ reduction potential [53]) shows an identical order of oxidation amount, with minimal corrosion for siliconized specimens (Supplementary Fig. 23). These results align well with the predicted phase stabilities in Fig. 5, which indicate that boride and silicide coatings are difficult to dissolve in molten chloride salts and, when present as compact, adherent layers, serve as barriers that protect the metal substrate.

We note that, while the thermal drying protocol employed in this work reduces the moisture content and volatile contaminants, thermal drying alone rarely removes all H_2O from highly hygroscopic molten chlorides, such as $MgCl_2$. In the absence of more aggressive chemical purification steps, residual moisture or hydroxyl species are typically expected to remain, alongside other nonvolatile species such as dissolved metal chlorides and oxide/oxychloride impurities. As a result, the absolute corrosion potentials and corrosion rates reported here are specific to the impurity inventory associated with our drying conditions and may differ from values obtained in other highly purified or contaminated melts. Specifically, residual oxygen-bearing impurities, such as hydroxide species generated from residual moisture, increase the oxidizing power of the melt and provide additional cathodic reduction pathways. This effect elevates the absolute corrosion currents, as previously demonstrated by the linear dependence of reduction peak currents on $MgOH^+$ concentrations [54]. However, all static corrosion tests and electrochemical measurements for a given salt composition were carried out using salts subjected to the same thermal pretreatment, so the influence of residual impurities is expected to be largely common to all specimens. Thus, while the absolute electrochemical values should be interpreted in the context of this impurity level, we do not expect these residual impurities to alter the relative ranking of corrosion resistance among the coatings or the mechanistic trends inferred from the impurity-inclusive phase-stability diagrams.

Beyond corrosion and thermodynamic stability, mechanical robustness under thermal and mechanical shock is an important practical concern when proposing these materials as potential coatings, because many ceramic or ceramic-rich layers can be intrinsically brittle. In this work, we focus on phase stability and molten-salt corrosion behavior. Yet, our preliminary results from nano-indentation and progressive-load scratch tests on siliconized SS316L show reduced hardness and modulus relative to bare SS316L [55] and a residual scratch depth of only ~45 % of the maximum penetration (i.e., ~55 % elastic recovery). These results clearly indicate that the diffusion-formed, graded Si layer does not behave as an extremely brittle ceramic film [56,57]. At the same time, intralayer defects and microstructural heterogeneity within diffusion-formed coatings may act as local stress-concentration sites under severe loading. Accordingly, in the present paper we restrict ourselves to this brief qualitative discussion; a systematic mechanical and thermal-shock qualification of these coatings is therefore required for practical deployment, and this more comprehensive assessment will be reported in follow-up work.

4. Conclusion

Here, we present the framework for multidimensional thermodynamic stability diagrams in molten salts and apply them to design corrosion-resistant ceramic coatings in molten chlorides. This framework incorporates the effects of critical impurities such as water into assessing phase stability in molten salts. The critical impurity levels, translated into effective moisture content through dissociation equilibrium, potentially serve as guidelines for salt purification. The predicted ceramic coatings are validated experimentally in terms of corrosion resistance. The framework is formulated for purified chloride melts in sealed or quasi-sealed configurations, and its extension to flowing or open systems-with spatially varying redox conditions and explicit control of the Cl_2/Cl^- couple-is left for future work. The framework opens avenues for understanding how metals and ceramics interact with

molten salt in realistic service conditions where hydrogen/tritium may originate from transmutation or adventitious impurities, and aid in developing industrial applications with molten salts.

CRediT authorship contribution statement

Seongwon Ham: Writing – original draft, Visualization, Software, Investigation, Formal analysis, Data curation. **Choah Kwon:** Software, Methodology, Investigation, Formal analysis, Conceptualization. **Minho Kim:** Investigation. **Han Lim Cha:** Investigation, Formal analysis, Data curation. **Ho-A Kim:** Investigation. **Jong-Il Yun:** Investigation. **Jun Woo Park:** Investigation. **Jongwoo Lee:** Validation. **SeungYop Paek:** Validation. **Jinsuo Zhang:** Conceptualization. **Ju Li:** Writing – review & editing, Supervision, Funding acquisition, Conceptualization. **Sangtae Kim:** Writing – review & editing, Writing – original draft, Visualization, Supervision, Project administration, Funding acquisition, Conceptualization.

Declaration of competing interest

The authors declare that they have no known competing financial interests or personal relationships that could have appeared to influence the work reported in this paper.

Acknowledgement

This work was supported by the National Research Foundation of Korea (NRF), funded by the Ministry of Science and ICT, the Republic of Korea (RS-2023-00261146) and by the Human Resources Development of the Korea Institute of Energy Technology Evaluation and Planning (KETEP) grant funded by the Korea government Ministry of Climate, Energy and Environment (RS-2024–00439210, No. RS-2024–00401407). This work was partly supported by Institute of Information & communications Technology Planning & Evaluation (IITP) grant funded by the Korea government(MSIT) (No. 2020–0–01373, Artificial Intelligence Graduate School Program(Hanyang University)) and the research fund of Hanyang University (HY-202100000660005). The computational resources from KISTI Supercomputing Center are acknowledged (KSC-2025-CRE-0281). JL and JSZ acknowledge support by the Department of Energy, Office of Nuclear Energy, Nuclear Energy University Program (NEUP) under Award Number DE-NE0009482. This material is based upon work supported by the Department of Energy National Nuclear Security Administration through Defense Nuclear Nonproliferation's Enabling Capabilities in Technology Consortium under Award Number DE-NA0004197. This report was prepared as an account of work sponsored by an agency of the United States Government. Neither the United States Government nor any agency thereof, nor any of their employees, makes any warranty, express or limited, or assumes any legal liability or responsibility for the accuracy, completeness, or usefulness of any information, apparatus, product or process disclosed, or represents that its use would not infringe privately owned rights. Reference herein to any specific commercial product, process, or service by trade name, trademark, manufacturer, or otherwise does not necessarily constitute or imply its endorsement, recommendation, or favoring by the United States Government or any agency thereof. The views and opinions of authors herein do not necessarily state or reflect those of the United States Government or any agency thereof.

Supplementary materials

Supplementary material associated with this article can be found, in the online version, at doi:10.1016/j.actamat.2026.122063.

References

[1] Q. Pang, J. Meng, S. Gupta, X. Hong, C.Y. Kwok, J. Zhao, Y. Jin, L. Xu, O. Karahan, Z. Wang, S. Toll, L. Mai, L.F. Nazar, M. Balasubramanian, B. Narayanan, D. R. Sadoway, Fast-charging aluminium-chalcogen batteries resistant to dendritic shorting, Nature 608 (2022) 704–711, https://doi.org/10.1038/s41586-022-04983-9.

[2] M. Liu, N.H. Steven Tay, S. Bell, M. Belusko, R. Jacob, G. Will, W. Saman, F. Bruno, Review on concentrating solar power plants and new developments in high temperature thermal energy storage technologies, Renew. Sustain. Energy Rev. 53 (2016) 1411–1432, https://doi.org/10.1016/j.rser.2015.09.026.

[3] B. Jo, D. Banerjee, Enhanced specific heat capacity of molten salt-based nanomaterials: effects of nanoparticle dispersion and solvent material, Acta Mater. 75 (2014) 80–91, https://doi.org/10.1016/j.actamat.2014.05.005.

[4] R. Roper, M. Harkema, P. Sabharwall, C. Riddle, B. Chisholm, B. Day, P. Marotta, Molten salt for advanced energy applications: a review, Ann. Nucl. Energy 169 (2022) 108924, https://doi.org/10.1016/j.anucene.2021.108924.

[5] S.J. Zinkle, G.S. Was, Materials challenges in nuclear energy, Acta Mater. 61 (2013) 735–758, https://doi.org/10.1016/j.actamat.2012.11.004.

[6] W. Han, W. Wang, H. Li, Y. Zhao, Y. Wang, R. Liu, M. Li, Electrochemical recovering Zr from molten salt using an Fe electrode, ACS Sustain. Chem. Eng. 9 (2021) 17393–17402, https://doi.org/10.1021/acssuschemeng.1c06931.

[7] S.G. Heo, J.Y. Yang, S.J. Oh, S.-J. Seo, M.H. Lee, K.-T. Park, Extraction of rare earth elements from neodymium (NdFeB) magnet scrap using magnesium halides, J. Rare Earths 43 (2025) 371–376, https://doi.org/10.1016/j.jre.2024.01.012.

[8] H. Hua, K. Yasuda, Y. Norikawa, T. Nohira, Highly efficient and precise rare-earth elements separation and recycling process in molten salt, Engineering 45 (2025) 165–173, https://doi.org/10.1016/j.eng.2022.12.013.

[9] S.-J. Ha, Y.K. Moon, H.-A. Cha, J.-J. Choi, B.-D. Hahn, S.-H. Choi, I.-R. Yoo, K.-H. Cho, K.-S. Moon, C.-W. Ahn, Fundamental study to grow single crystals with high performances operated up to high temperatures in donor-doped materials for energy harvesting, Acta Mater. 295 (2025) 121180, https://doi.org/10.1016/j.actamat.2025.121180.

[10] X.-H. Wang, H. Gu, Q.-W. Huang, M. Čeh, Cation occupancy at the A1/A2 sites in strontium barium niobate micro-crystals grown from molten NaCl and KCl salts, Acta Mater. 55 (2007) 5304–5309, https://doi.org/10.1016/j.actamat.2007.04.041.

[11] S.K. Gupta, Y. Mao, A review on molten salt synthesis of metal oxide nanomaterials: status, opportunity, and challenge, Prog. Mater. Sci. 117 (2021) 100734, https://doi.org/10.1016/j.pmatsci.2020.100734.

[12] R. Littlewood, Diagrammatic representation of the thermodynamics of metal-fused chloride systems, J. Electrochem. Soc. 109 (1962) 525, https://doi.org/10.1149/1.2425462.

[13] H. Lux, "Säuren" und "Basen" im schmelzfluss: die bestimmung der Sauerstoffionen-konzentration, Zeitschrift Für Elektrochemie Und Angewandte Physikalische Chemie 45 (1939) 303–309, https://doi.org/10.1002/bbpc.19390450405.

[14] M.D. Ingram, G.J. Janz, The thermodynamics of corrosion in molten carbonates: application of *E*/pCO2 diagrams, Electrochim. Acta 10 (1965) 783–792, https://doi.org/10.1016/0013-4686(65)80043-3.

[15] H.S. Swofford, P.G. McCormick, An electrochemical study of nitrite and oxide in sodium nitrate-potassium nitrate eutectic melts, Anal. Chem. 37 (1965) 970–974, https://doi.org/10.1021/ac60227a005.

[16] G. Bombara, G. Baudo, A. Tamba, Thermodynamics of corrosion in fused sulphates, Corros. Sci. 8 (1968) 393–404, https://doi.org/10.1016/S0010-938X(68)90048-6.

[17] R. Combes, J. Vedel, B. Trémillon, Mesure de pO2- au moyen d'une electrode a membrane de zircone stabilisee et determination potentiometrique de constantes d'equilibre d'echange de O2- dans le melange equimolaire NaCl-KCl fondu, Electrochim. Acta 20 (1975) 191–200, https://doi.org/10.1016/0013-4686(75)85024-9.

[18] Y. Kanzaki, M. Takahashi, The oxygen electrode in fused lithium chloride-potassium chloride eutectic containing oxide ion, J. Electroanal. Chem. Interfacial. Electrochem. 58 (1975) 339–348, https://doi.org/10.1016/S0022-0728(75)80091-X.

[19] A. Conte, M.D. Ingram, Corrosion of silver in fused nitrates: applications of *E*/pO2-diagrams, Electrochim. Acta 13 (1968) 1551–1557, https://doi.org/10.1016/0013-4686(68)80138-0.

[20] T. Ishitsuka, K. Nose, Solubility study on protective oxide films in molten chlorides created by refuse incineration environment, Mater. Corros. 51 (2000) 177–181, https://doi.org/10.1002/(SICI)1521-4176(200003)51:3%253C177::AID-MACO177%253E3.0.CO;2-O.

[21] J.W. Koger, Chromium depletion and void formation in Fe-Ni-Cr alloys during molten salt corrosion and related processes, in: M.G. Fontana, R.W. Staehle (Eds.), Advances in Corrosion Science and Technology, Springer US, Boston, MA, 1974: pp. 245–318. https://doi.org/10.1007/978-1-4615-9059-0_4.

[22] S. Guo, J. Zhang, W. Wu, W. Zhou, Corrosion in the molten fluoride and chloride salts and materials development for nuclear applications, Prog. Mater. Sci. 97 (2018) 448–487, https://doi.org/10.1016/j.pmatsci.2018.05.003.

[23] B.C. Kelleher, S.F. Gagnon, I.G. Mitchell, Thermal gradient mass transport corrosion in NaCl-MgCl 2 and MgCl 2 -NaCl-KCl molten salts, Mater. Today Commun. 33 (2022) 104358, https://doi.org/10.1016/j.mtcomm.2022.104358.

[24] K. Sridharan, T.R. Allen, 12 - Corrosion in Molten Salts, in: F. Lantelme, H. Groult (Eds.), Molten Salts Chemistry, Elsevier, Oxford, 2013: pp. 241–267. https://doi.org/10.1016/B978-0-12-398538-5.00012-3.

[25] S.S. Raiman, S. Lee, Aggregation and data analysis of corrosion studies in molten chloride and fluoride salts, J. Nucl. Mater. 511 (2018) 523–535, https://doi.org/10.1016/j.jnucmat.2018.07.036.
[26] T. Ghaznavi, S.Y. Persaud, R.C. Newman, Electrochemical corrosion studies in molten chloride salts, J. Electrochem. Soc. 169 (2022) 061502, https://doi.org/10.1149/1945-7111/ac735b.
[27] Y. Peng, K.K. Bawane, X. Liu, X. Zheng, M. Ge, X. Xiao, E.M. Kim, P. W. Halstenberg, S. Dai, J.F. Wishart, Y.K. Chen-Wiegart, Unraveling impurity-dependent morphological and chemical evolution of Ni-20Cr alloy in eutectic LiCl-KCl molten salt, ACS. Appl. Mater. Interfaces. 17 (2025) 28764–28776, https://doi.org/10.1021/acsami.4c23034.
[28] B. D'Souza, A. Leong, Q. Yang, J. Zhang, Corrosion behavior of boronized nickel-based alloys in the molten chloride Salt, Corros. Sci. 182 (2021) 109285, https://doi.org/10.1016/j.corsci.2021.109285.
[29] B.O. Okonkwo, C. Kim, T. An, C. Jang, D. Kang, W. Yang, S. Choi, Corrosion behaviour of Al-containing alloys in Cl-based molten salt environment, J. Nucl. Mater. 599 (2024) 155207, https://doi.org/10.1016/j.jnucmat.2024.155207.
[30] X. Luo, Z. Ning, L. Zhang, R. Lin, H. He, J. Yang, Y. Yang, J. Liao, N. Liu, Influence of Al2O3 overlay on corrosion resistance of plasma sprayed yttria-stabilized zirconia coating in NaCl-KCl molten salt, Surf. Coat. Technol. 361 (2019) 432–437, https://doi.org/10.1016/j.surfcoat.2019.01.054.
[31] E.O. Blair, D.K. Corrigan, H.J. Levene, I. Schmueser, J.G. Terry, S. Smith, A. R. Mount, A.J. Walton, Improving the yield and lifetime of microfabricated sensors for harsh environments, IEEE Trans. Semicond. Manuf. 30 (2017) 192–200, https://doi.org/10.1109/TSM.2017.2715377.
[32] L. Swain, G. Pakhui, A. Jain, S. Ghosh, Electrochemical behaviour of LiCl-KCl eutectic melts containing moisture as impurity. Part I: inert tungsten electrode, J. Electroanal. Chem. 910 (2022) 116125, https://doi.org/10.1016/j.jelechem.2022.116125.
[33] A. Jain, S.P. Ong, G. Hautier, W. Chen, W.D. Richards, S. Dacek, S. Cholia, D. Gunter, D. Skinner, G. Ceder, K.A. Persson, Commentary: the Materials Project: a materials genome approach to accelerating materials innovation, APL. Mater. 1 (2013) 011002, https://doi.org/10.1063/1.4812323.
[34] S. Takamoto, C. Shinagawa, D. Motoki, K. Nakago, W. Li, I. Kurata, T. Watanabe, Y. Yayama, H. Iriguchi, Y. Asano, T. Onodera, T. Ishii, T. Kudo, H. Ono, R. Sawada, R. Ishitani, M. Ong, T. Yamaguchi, T. Kataoka, A. Hayashi, N. Charoenphakdee, T. Ibuka, Towards universal neural network potential for material discovery applicable to arbitrary combination of 45 elements, Nat. Commun. 13 (2022) 2991, https://doi.org/10.1038/s41467-022-30687-9.
[35] S. Takamoto, D. Okanohara, Q.-J. Li, J. Li, Towards universal neural network interatomic potential, J. Materiomics 9 (2023) 447–454, https://doi.org/10.1016/j.jmat.2022.12.007.
[36] B. Fultz, Vibrational thermodynamics of materials, Prog. Mater. Sci. 55 (2010) 247–352, https://doi.org/10.1016/j.pmatsci.2009.05.002.
[37] L. Wang, T. Maxisch, G. Ceder, Oxidation energies of transition metal oxides within the $\mathrm{GGA}+\mathrm{U}$ framework, Phys. Rev. B 73 (2006) 195107, https://doi.org/10.1103/PhysRevB.73.195107.
[38] K.A. Persson, B. Waldwick, P. Lazic, G. Ceder, Prediction of solid-aqueous equilibria: scheme to combine first-principles calculations of solids with experimental aqueous states, Phys. Rev. B 85 (2012) 235438, https://doi.org/10.1103/PhysRevB.85.235438.
[39] S. Guo, N. Shay, Y. Wang, W. Zhou, J. Zhang, Measurement of europium (III)/europium (II) couple in fluoride molten salt for redox control in a molten salt reactor concept, J. Nucl. Mater. 496 (2017) 197–206, https://doi.org/10.1016/j.jnucmat.2017.09.027.
[40] W. Ding, A. Bonk, T. Bauer, Corrosion behavior of metallic alloys in molten chloride salts for thermal energy storage in concentrated solar power plants: a review, Front. Chem. Sci. Eng. 12 (2018) 564–576, https://doi.org/10.1007/s11705-018-1720-0.
[41] C. Mejia, D. Rappleye, Investigation of a stable and saturated reference electrode using metal chlorides and oxides in eutectic LiCl-KCl molten salts, Nucl. Eng. Technol. 58 (2026) 103875, https://doi.org/10.1016/j.net.2025.103875.
[42] C. Mejia, N. Christensen, R.R. Ceron, D. Rappleye, Development of a stable and buffered reference electrode for binary molten chlorides salts, Electrochim. Acta 512 (2025) 145496, https://doi.org/10.1016/j.electacta.2024.145496.
[43] O. Shirai, T. Nagai, A. Uehara, H. Yamana, Electrochemical properties of the Ag+| Ag and other reference electrodes in the LiCl-KCl eutectic melts, J. Alloys. Compd. 456 (2008) 498–502, https://doi.org/10.1016/j.jallcom.2007.02.104.
[44] D. Yoon, A. Baggett, S. Phongikaroon, J.A. King, K. Marsden, Fundamental data acquisition toward silver-silver chloride reference electrode, J. Electrochem. Soc. 166 (2019) E159–E164, https://doi.org/10.1149/2.0721906jes.
[45] M. Zhang, J. Ge, J. Zhang, L.E. Liu, Redox potential measurement of AgCl in molten LiCl-KCl salt using chronopotentiometry and potentiodynamic scan techniques, Electrochem. Commun. 105 (2019) 106498, https://doi.org/10.1016/j.elecom.2019.106498.
[46] J.W. Park, S. Yoon, H.J. Eom, S. Kim, C. Jang, J.-I. Yun, Formation of UO2 on stainless steel 316 corroded in NaCl-KCl-UClx (x = 3,4) salts: effect of crucible material, Corros. Sci. 252 (2025) 112979, https://doi.org/10.1016/j.corsci.2025.112979.
[47] S.S. Raiman, J.M. Kurley, D. Sulejmanovic, A. Willoughby, S. Nelson, K. Mao, C. M. Parish, M.S. Greenwood, B.A. Pint, Corrosion of 316H stainless steel in flowing FLiNaK salt, J. Nucl. Mater. 561 (2022) 153551, https://doi.org/10.1016/j.jnucmat.2022.153551.
[48] K. Rippy, L. Witteman, P.R. Taylor, J.C. Vidal, Predicting and understanding corrosion in molten chloride salts, MRS. Adv. 8 (2023) 855–859, https://doi.org/10.1557/s43580-023-00642-x.
[49] Y. Ito, T. Goto, Electrochemistry of nitrogen and nitrides in molten salts, J. Nucl. Mater. 344 (2005) 128–135, https://doi.org/10.1016/j.jnucmat.2005.04.030.
[50] S.-H. Cho, B.-H. Park, J.-M. Hur, H.-S. Lee, K.-C. Song, J.-H. Lee, Corrosion behaviour of Y2O3-ZrO2 coatings on IN713LC in a LiCl-Li2O molten salt, Corros. Sci. 52 (2010) 2353–2364, https://doi.org/10.1016/j.corsci.2010.03.020.
[51] J.C. Gomez-Vidal, Corrosion resistance of MCrAlX coatings in a molten chloride for thermal storage in concentrating solar power applications, NPJ. Mater. Degrad. 1 (2017) 7, https://doi.org/10.1038/s41529-017-0012-3.
[52] S. Yoon, S. Choi, Spectroelectrochemical behavior of Cr, Fe, Co, and Ni in LiCl-KCl molten salt for decontaminating radioactive metallic wastes, J. Electrochem. Soc. 168 (2021) 013504, https://doi.org/10.1149/1945-7111/abdc7e.
[53] P. Masset, D. Bottomley, R. Konings, R. Malmbeck, A. Rodrigues, J. Serp, J.-P. Glatz, Electrochemistry of uranium in molten LiCl-KCl eutectic, J. Electrochem. Soc. 152 (2005) A1109, https://doi.org/10.1149/1.1901083.
[54] W. Ding, A. Bonk, J. Gussone, T. Bauer, Electrochemical measurement of corrosive impurities in molten chlorides for thermal energy storage, J. Energy Storage 15 (2018) 408–414, https://doi.org/10.1016/j.est.2017.12.007.
[55] W.C. Oliver, G.M. Pharr, An improved technique for determining hardness and elastic modulus using load and displacement sensing indentation experiments, J. Mater. Res. 7 (1992) 1564–1583, https://doi.org/10.1557/JMR.1992.1564.
[56] A. Leyland, A. Matthews, On the significance of the H/E ratio in wear control: a nanocomposite coating approach to optimised tribological behaviour, Wear. 246 (2000) 1–11, https://doi.org/10.1016/S0043-1648(00)00488-9.
[57] S.J. Bull, Failure mode maps in the thin film scratch adhesion test, Tribol. Int. 30 (1997) 491–498, https://doi.org/10.1016/S0301-679X(97)00012-1.